Influences of cation distribution on proton insertion dynamics in complex spinel $NiCo_2O_4$ thin films via ionic liquid gating

Meng Wu,[1,*] Xiaochun Huang,[2] Yihuan Li,[1] Hao Luo,[1] Jueli Shi,[2] Kelvin H. L. Zhang,[2,†] Tielong Deng,[1] Ying Du,[1] Hui-Qiong Wang,[1] and Junyong Kang[1]

[1]*Engineering Research Center of Micro-nano Optoelectronic Materials and Devices, Ministry of Education, Fujian Key Laboratory of Semiconductor Materials and Applications, CI Center for OSED, and Department of Physics, Xiamen University, Xiamen 361005, People's Republic of China*

[2]*State Key Laboratory of Physical Chemistry of Solid Surfaces, College of Chemistry and Chemical Engineering, Xiamen University, Xiamen 361005, People's Republic of China*

(Received 16 May 2023; revised 1 July 2023; accepted 7 July 2023; published 17 July 2023)

Ionic liquid gating (ILG) induced proton doping has appeared as an efficient tuning knob to manipulate novel ground states and realize rich applications in complex spinel oxides. We report insights into the influences of cation distribution on local atomic and electronic structure of $NiCo_2O_4$ (NCO) epitaxial films as well as its correlation with proton insertion dynamics. For NCO films deposited at lower oxygen partial pressure (P_{O_2}), we verify the dominant structural variation as cation distribution rather than oxygen vacancies through electric and magnetic transport analyses. The x-ray absorption spectra at the O K-edge further suggests two couples of cation inversion at octahedral (O_h)-Ni^{2+} and tetrahedral (T_d)-Co^{2+} sites, resulting in Ni^{3+} at T_d and more Co^{3+} at O_h sites. Through systematic investigations of the structural and valence states of NCO films with different ILG treatment conditions, our results display the robust ionic reduction procedure, i.e., the Ni ions near the Fermi level exhibit a prior Ni^{3+} to Ni^{2+} reduction whereas the Co ions at different coordinated sites show the gradual $Co^{3+} \rightarrow Co^{2+}$ reduction procedure. However, more stringent conditions are necessary for fully protonating NCO films deposited at low P_{O_2}, which can be ascribed to the short relaxation time and poor diffusion coefficient accompanying with the increased cation disorders.

DOI: 10.1103/PhysRevMaterials.7.075001

I. INTRODUCTION

The ionic liquid gating (ILG) technique offering the new ionic degree of freedom has attracted considerable research attention in the field of quantum materials recently, where the gating electric field and the mobile ions serve as efficient tuning knobs to control the ground state properties, enabling novel emergent phenomena such as metal-insulator transition [1,2], magnetism [3], and superconductivity [4–6], etc. Two mechanisms known as the electrostatic and the electrochemical mechanism may dominate in the ILG approach as illustrated in Fig. 1(a). In the latter case, the mobile ions, i.e., H^+ or O^{2-}, originate from the hydrolysis of residual H_2O inside the electrolyte, transport across the interface, and permeate into the oxides. Particularly, the doping of protons (H^+) with the smallest ionic radius emerges as the ideal candidate to engineer the ground state properties, where the protonated functional materials further offer the potential electronic and spintronic applications. ILG induced proton incorporation into transition metal oxide systems can be generally realized through the topotactic transition, which retains the parent lattice framework and the biaxial strain effect, making them particular as neat systems for the studies of proton dynamics and the underlying mechanism of novel quantum states [7–12]. Among the protonation in various systems, spinel complex oxides are peculiar where the multiple transition metal ions with different electronic configurations and coordinations allow diverse possibilities for manipulating the ground states and realizing potential applications.

For the NCO of interest here, it exhibits an inverse spinel structure with the chemical formula as $[Co^{3+}]_{T_d}[Ni^{2+}Co^{3+}]_{O_h}O_4$ ideally, where the tetrahedral (T_d) site is occupied by Co^{3+} ions, and the octahedral (O_h) site is equally occupied by Ni^{2+} and Co^{3+} ion, as illustrated in Fig. 1(b). Moreover, the multifunctional properties of NCO strongly depend on the synthesis conditions, which can drive the mixed valence state, antisite cation distribution and other point defects therein [13–15]. Practically, the coordination formula can be expressed as $[Co^{3+}_{1-\delta}Co^{2+}_{\delta}]_{T_d}[Ni^{2+}_{1-\delta}Ni^{3+}_{\delta}Co^{3+}]_{O_h}O_4$ [16,17]. For instance, previous reports have shown that the deposition temperature and oxygen partial pressure (P_{O_2}) in pulsed laser deposition (PLD) technique can largely affect the electromagnetic properties. We reported the deposition temperature affected ground state variations from metallic ferromagnetic to insulating nonmagnetic, which can be ascribed to the crucial role of Ni^{3+} with a delocalized $3d$ derived electronic state near the Fermi level (E_f) at low temperatures [18]. Furthermore, cation distribution in NCO films strongly depends on P_{O_2}. For P_{O_2} above 100 mTorr, the cation distribution is close to

*m.wu@xmu.edu.cn
†Kelvinzhang@xmu.edu.cn

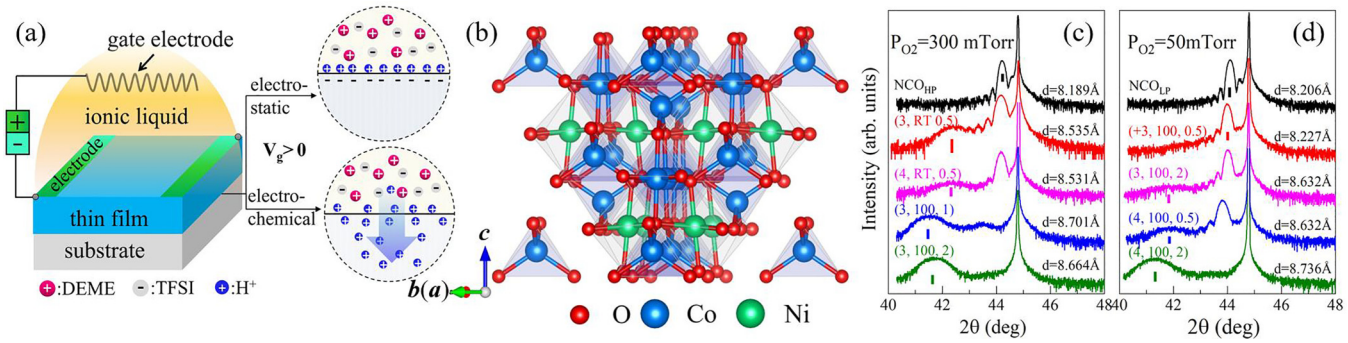

FIG. 1. Panel (a): schematic illustration of the ILG experimental setup. In response to the positively gated voltage, the protons (H^+) originated from the hydrolysis of residual H_2O inside the IL accumulate at the electrolyte-oxide interface. Magnified views of at the interfaces are illustrated with two dominant mechanisms, i.e., the electrostatic and the electrochemical mechanism where protons permeate across the interface toward the oxides. Panels (c)–(d) show the x-ray diffraction scans along the specular direction for (c) NCO_{HP}(P_{O_2} = 300 mTorr) and for (d) NCO_{LP} (P_{O_2} = 50 mTorr) sets of films at different ILG conditions as labeled in the corresponding spectrum, respectively. The ILG experimental conditions are labeled as (A, B, C), with A, B, C denoting the positively applied voltage value (3 or 4 V), the temperature (RT or 100 °C), as well as the treatment period in unit of hour, respectively. The calculated out-of-plane lattice constants from the characteristic peak marked as short lines are also listed in each spectrum.

the stoichiometric, whereas films exhibit the deterioration of ferromagnetic properties for P_{O_2} below 100 mTorr [19,20].

ILG-manipulated metallic ferromagnetic (pristine NCO) to insulating antiferromagnetic (two-proton containing H_2NCO phase) transitions had been reported in spinel the NCO system previously [21]. Recently, we provided the detailed electromagnetic and valence state evolutions in NCO films with the ideal stoichiometry, where the Ni ions near the E_f show the prior $Ni^{3+} \rightarrow Ni^{2+}$ reduction and the Co ions exhibit a stepwise $Co^{3+} \rightarrow Co^{2+}$ [22]. Furthermore, the intermediate proton-doped NCO films (with protons less than two per f.u.) exhibit the exchange bias effect that is absent in pristine NCO films, which sheds light on the manipulation of the exchange bias effect for spintronic applications in complex oxides via ILG-controlled protonation. Therefore, toward manipulating the novel ground states in complex oxides and effectively utilizing them in emerging technologies, a microscopic understanding of the cation distribution, defects, local atomic coordination, electronic structure, as well as their influences on proton insertion dynamics, are of vital importance, which is the focus of present work.

II. EXPERIMENTAL DETAILS

NCO (bulk lattice constant a_{NCO} = 8.116 Å) thin films were deposited on single crystal $MgAl_2O_4$(004) (MAO, a_{MAO} = 8.083 Å) substrates using the PLD technique. The MAO target was ablated by a focused KrF excimer laser (λ = 248 nm) beam with an energy density of 2.5 Jcm^{-2} at a repetition rate of 10 H_z. NCO thin films with thickness of ≈ 40 nm were grown at a substrate temperature of 350 °C with different P_{O_2}, i.e., P_{O_2} = 50 mTorr or 300 mTorr. After the deposition, the temperature was lowered with a constant ramp rate of 25 °C/min to room temperature while the pressure remained unchanged. The crystal structure and epitaxial relationship of the investigated films were determined by high-resolution XRD specular scans. Electrical resistivity measurements were performed using the Van der Pauw geometry with Au contacts in the temperature range of 10–300 K. Magnetic measurements were performed using a Quantum Design SQUID magnetometer.

During the ILG gating, the prepared NCO films were placed in a quartz crucible and covered with ionic liquid between the film surface and the screwed platinum gate electrode. The bottom electrode was prepared with a silver conductive adhesive on four edges of the NCO films. The crucible was heated to desired temperatures by a thermal heater below. The voltage was ramped to the desired 3 V or 4 V within about one minute and maintained for 0.5 h, 1 h, or 2 h. After removing the gate voltage, the setup cooled down to room temperature naturally. The TOF-SIMS (time-of-flight secondary-ion mass spectrometry setup from GmbH, Germany) measurements had been performed to provide direct information about hydrogen incorporation and concentrations. The caesium ion beam was used as the sputtering beam with energy of 1 keV at an incident angle of 45° and a sputtering rate of about 0.13 nm/s calibrated for SiO_2, which is capable for collecting the ions with atomic mass between 0–900 amu. We further estimate a sputtering rate of about 0.093 nm/s for NCO thin films, taking into account a total thickness of ≈ 40 nm. The electronic structures of thin films were further probed by synchrotron-based XAS measurements in the total electron yield mode at the Magnetic Circular Dichroism beamline (BL12B) of the National Synchrotron Radiation Laboratory (NSRL), Hefei, and the 4B9B beamline at Beijing Synchrotron Radiation Facility (BSRF).

III. RESULTS AND DISCUSSIONS

A. ILG of NCO thin films and structural characterizations

Two sets of NCO thin films were grown on MAO substrates at different P_{O_2}. Figures 1(c)–1(d) show the XRD scans along the specular direction of NCO thin films, where the pristine NCO_{HP} (denoting NCO films deposited with P_{O_2} = 300 mTorr) and NCO_{LP} (denoting NCO grown with P_{O_2} = 50 mTorr) show characteristic thickness fringes, indicating the high crystalline quality of the epitaxial films. From the read-off (004) diffraction angles, the out-of-plane lattice

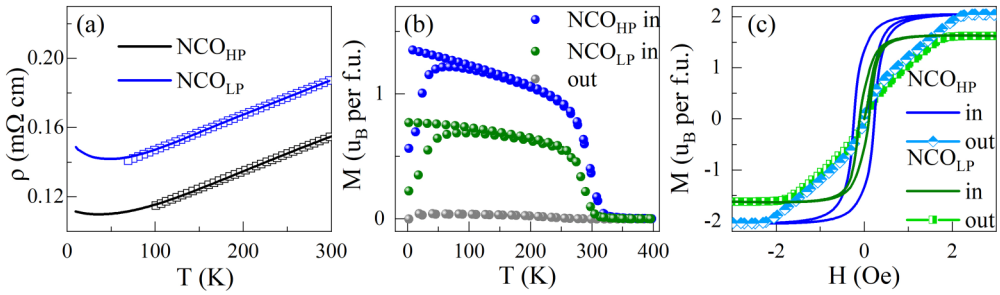

FIG. 2. Detailed electric and magnetic transport measurements to distinguish the existence of cation disorder or oxygen deficiency in NCO_{LP} thin film. Panel (a): temperature dependent resistivity curves; (b): temperature dependent magnetization curves along in-plane and out-of-plane directions; (c) magnetic hysteresis loops measured at 2 K for NCO_{HP} and NCO_{LP} thin films, respectively.

constant can be calculated. Both NCO_{HP} and NCO_{LP} pristine samples show a larger out-of-plane lattice parameter than the bulk value due to the compressive strain induced by MAO substrate.

A schematic view of the ILG experimental setup is shown in Fig. 1(a), using the as-received N,N-diethyl-N-(2-methoxyethyl)-N-methylammoniumbistrifluoromethy lsulphonyl-imide (DEME-TFSI) as the electrolyte. Applying the positively gated voltage, the protons (H^+) originated from the hydrolysis of residual H_2O inside the IL accumulate at the electrolyte-oxide interface with the chemical reaction as $H_2O \rightarrow 2\,H^+ + O^{2-}$; $x\,H^+ + NiCo_2O_4 \rightarrow H_xNiCo_2O_4$ ($0 < x \leqslant 2$).

With changing the gating voltage, temperature, and periods, the pristine NCO_{HP} films change to the intermediate states with a mixture of two phases [with treatment conditions as (3, RT, 0.5), (4, RT, 0.5)] and eventually to the fully protonated films with approximately two proton per f.u. with treatment conditions as (3, 100, 2). We note that the ILG experimental conditions are labeled as (A, B, C), with A, B, C denoting the positively applied voltage value (three or four) in unit of V, the temperature (RT or 100 °C) as well as the treatment period in units of hour, respectively. The (3, 100, 2) treated NCO_{HP} films with calculated lattice constant of $\approx$ 8.664 Å have been identified as two-proton incorporated H_2NCO [21]. Since the expansion of lattice parameters increases monotonously with the increased proton concentration in the lattice [23], the films in the intermediate states exhibiting a small lattice constant of $\approx$ 15%, (i.e., $|8.533\text{-}8.664|/8.664$) corresponds to the H_xNCO phase with averaged $0 < x < 2$.

For the NCO_{LP} thin films, after applying +3 V gating voltage at an elevated temperature of 100 °C for 2 h, which are exactly the same as these applied to obtain H_2NCO_{HP} films, interestingly the NCO_{LP} (3, 100, 2) films show a mixture of the pristine NCO phase and the new phase appearing at $\approx$ 41.82° with a larger out-of-plane lattice parameter of $\approx$ 8.632 Å. A similar two phase structure has also been observed for an increased voltage of (4, 100, 0.5). After increasing the gating period up to 2 h, the whole film entirely changed to a new phase at $\approx$ 41.33° with obtained lattice constant of $\approx$ 8.736 Å. Therefore, compared to NCO_{HP} thin films, more stringent conditions are necessary for full protonation of NCO_{LP} thin films as suggested by the structure analyses. Besides, we note that all the protonated samples, including the mixture phase (H_xNCO and NCO phase) as well as the two-proton incorporated H_2NCO phase remains unchanged at ambient conditions for months, indicating that the phase transformations are stable.

B. Cation disorder or oxygen deficiency in NCO_{LP} films

Before providing the detailed insights on proton incorporation dynamics and their origins in NCO_{HP} and NCO_{LP} thin films, one essential question would be what is the dominant contribution induced by lower P_{O_2}? In principle, for NCO_{LP} films deposited at low P_{O_2}, both antisite defects and oxygen vacancies could be introduced to the system. In order to distinguish the major contribution, we provide detailed electric and magnetic transport measurements. Figure 2(a) exhibits the temperature dependent dc electrical resistivity curves. NCO_{HP} and NCO_{LP} pristine samples show metallic behaviors with a linear T dependence above 100 K, suggesting a normal electron-phonon coupling mechanism. The residual resistivity of NCO_{LP} is slightly higher than that of NCO_{HP}, which is similar as reported in literature and has been ascribed to the increased amount of cation disorders [19,24]. The low temperature resistivity upturn can be related to the defects or disorders. To verify the contribution from oxygen vacancies, we annealed the NCO films after thin film deposition at oxygen condition, the resistivity of the annealed films remains comparable as the as-grown NCO film. This suggests that the existence of oxygen vacancies might not be the main difference between NCO_{HP} and NCO_{LP} films.

Figures 2(b) and 2(c) show the temperature dependent magnetization (M-T) curves and the magnetic hysteresis (M-H) loops, respectively. The diamagnetic signal was subtracted by linearly fitting the M-H data at larger magnetic fields. For pristine NCO thin films, Fig. 2(b) compares the zero-field cooling and field cooling (at 100 Oe) M-T curves along in-plane and out-of-plane directions for NCO_{HP} and NCO_{LP}, respectively. NCO_{HP} shows the paramagnetic to ferromagnetic transition at $T_c \approx 320$ K, which is compared to the value reported in literature for NCO thin films [25]. NCO_{LP} shows a slightly smaller magnetic transition temperature with $T_c \approx 300$ K. The reduced T_c phenomenon has been reported previously in offstoichiometric [19] and in oxygen deficient NCO thin films as well [24], implying the possible existence of both contributions in NCO_{LP} films. Moreover, the saturated magnetization of NCO_{HP} is $\approx$ 2 μ_B/f.u. at 2 K, which is consistent with the theoretical value for stoichiometry NCO. The NCO_{LP} thin film shows a reduced magnetic moment about 1.6 μ_B/f.u. at 2 K. The out of plane magnetization

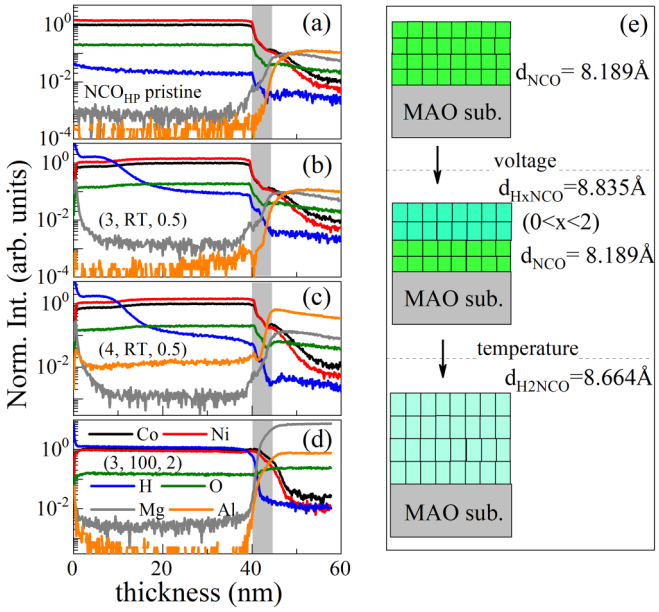

FIG. 3. The normalized intensity ratios of different ions obtained from TOF-SIMS measurements of (a) NCO_{HP} pristine, (b) NCO_{HP} (3, RT, 0.5), (c) NCO_{HP} (4, RT, 0.5), and (d) NCO_{HP} (3, 100, 2) films. Panel (e) illustrates the proton evolution process based on TOF-SIMS and XRD analyses.

of NCO_{HP} exhibits a typical ferromagnetic hysteresis loop with a coercive field H_c of 0.44 T, which value is reduced to $\approx$ 0.21 T for NCO_{LP} film. Moreover, the in-plane magnetization displays a negligibly small hysteresis which increases gradually with increasing the applied magnetic field. This behavior is known as the perpendicular magnetic anisotropy in literatures [25,26] and the saturated anisotropy field is $\approx$ 2.3 T for NCO_{HP} film. Similarly, NCO_{LP} film also shows the perpendicular magnetic anisotropy behavior whereas the in-plane saturated anisotropy field is decreased to $\approx$ 1.85 T. Suzuki *et al.* investigated the effects of oxygen vacancies on the perpendicular magnetic anisotropy and revealed that the magnetic anisotropy and the anisotropy field is independent on introducing oxygen vacancies [24]. The reduced anisotropy field, together with the insensitive of ρ-T behavior at different annealing oxygen pressure imply that the dominant structural variation in NCO_{LP} is cation disorder, rather than the oxygen deficiency.

C. Proton incorporation depth profile

TOF-SIMS experiments were performed to provide the distribution depth profiles of different ions in NCO thin films, as shown in Fig. 3. Since the absolute intensity values are not meaningful for TOF-SIMS measurements, the intensity ratios [i.e., I(A)/I(Co) with A denoting H, ^{18}O, Ni, Mg, and Al ions] are used for comparison. Figure 3 shows the SIMS spectra for NCO_{HP} pristine and different treated thin films. Both the normalized intensity ratios [I(H)/I(Co)] and the depth profiles of hydrogen ions change dramatically from NCO_{HP} pristine [Fig. 3(a)] to mixed phase [Figs. 3(b) and (c)] to fully protonated phase [Fig. 3(d)]. Quantitatively, the hydrogen distributes homogenously in NCO_{HP} pristine film with normalized I(H)/I(Co) intensity ratio, about 2%. For the treated NCO_{HP} (3, RT, 0.5) and (4, RT, 0.5) films with mixed pristine and new phases as shown in Figs. 3(b) and (c), the hydrogen ions exhibit enhanced ionic intensities as well as a stepwise depth profile. An enhanced amount of hydrogen ions accumulates at the top surface layers which extends about one third of the total thickness, whereas the hydrogen intensities at the layers below increase to about 10%, as shown in Fig. 3(b). With increasing the gating voltage to +4 V, there is no notable changes in hydrogen intensity profile compared to +3 V, implying that gating procedure, i.e., the hydrogen insertion and diffusion, reach a near equilibrium state. Upon increasing the temperature from RT to 100 °C, the hydrogen ions propagate and distribute homogeneously again with normalized I(H)/I(Co) ratio approximately two orders of magnitude higher than that of the pristine film. In contrast, the I(^{18}O)/I(Co) intensity ratios in the investigated films do not show obvious variations. Therefore, we conclude that the electrochemical mechanism dominates in NCO films, and the protons permeate into NCO thin films using ILG with positive bias. Meanwhile, the interfacial region with thickness of approximately 4.5 nm does not extend during the ILG treatments. The normalized I(Ni)/I(Co) intensity ratios exhibit no clear change, indicating that the voltage-driven ILG is a nondestructive topotactic process. The variation of the I(H)/I(Co) ratios, as well as the structural characterizations, provide us a clear picture of the proton evolution process, as illustrated in Fig. 3(e). Upon varying the ILG experimental conditions, NCO thin films exhibit a gradual proton evolution process, which change from pristine NCO to a mixed structure composed by protonated H_xNCO phase and pristine NCO phase, as well as eventually to a fully protonated new phase with H_2NCO chemical formula, as suggested by x-ray structural analyses. This proton insertion profile can be ascribed to the high proton insertion barrier and the poor proton diffusion coefficient [21].

D. Element-resolved electronic structure evolutions

Element-specified XAS measurements have been performed to investigate the local electronic structure variations for NCO_{HP} and NCO_{LP} films at different representative stages. Figures 4(a)–4(c) present the XAS results for NCO_{HP} pristine, (3, RT, 0.5), (3, 100, 0.5), and the fully protonated (3, 100, 2) H_2NCO samples at the Co L_{23} edge, Ni L_{23} edge, and O K edge, respectively. The XAS results on the pristine NCO_{HP} sample show a mixed valence state of 2+ and 3+ for both Ni and Co ions [Fig. 4(a)], which is consistent with our previous study, as well as in literatures [18,21]. Through the ILG treatments, the Ni ions show the prior valence state variations from the mixed Ni^{3+} and Ni^{2+} to reduced Ni^{2+} at the initial stage with (3, RT, 0.5) conditions. However, the Co ions exhibit a gradual valence state variation, i.e., the shift of the absorption peaks toward lower energies at (3, RT, 0.5) conditions featured by increased Co^{2+} contribution and eventually with the dominant Co^{2+} valence state in the fully protonated NCO_{HP} (3, 100 °C, 2) film, as shown in Fig. 4(a).

The spectral evolutions of the prepeak region at the O K edge with photon energy below $\approx$ 529 eV also reflect the proton insertion dynamics. The prepeak region can be classified as three peaks, labeled as I, II, III in Fig. 4(c). These three peaks in pristine NCO_{HP} films can be assigned to the

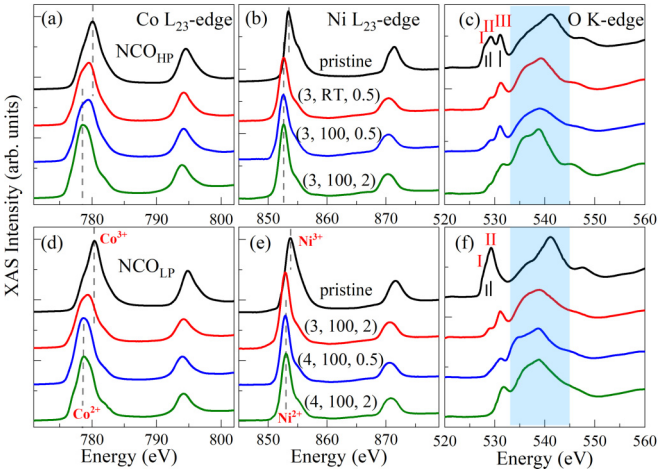

FIG. 4. XAS spectral evolutions for NCO_{HP} (a)–(c) and NCO_{LP} (d)–(f) series of films at the Co L_{23} edge, Ni L_{23} edge, and O K edge with treatment conditions labeled in the corresponding spectrum, respectively.

transition from O 1*s* to the unoccupied O 2*p* band mixed with Ni^{3+} e_g state, the O 2*p* state hybridized to the unoccupied Co 3*d* states in different O_h, and T_d coordination environments and the O 2*p*-Ni^{2+} hybridization state, respectively [18,22]. By changing the ILG treatment conditions, we observe the vanishing of peak I and the reduced peak intensity at peak II with (3, RT, 0.5) treatment, implying that the introduction of one additional electron due to proton incorporation resides at Ni^{3+} and partial at Co^{3+} states. This agrees well with the valence state variations at Ni and Co L_{23} edge. The peak intensity of peak II reduces after (3, 100, 0.5) treatment. In the fully protonated NCO_{HP} (3, 100, 2) phase, the prepeak regions are further suppressed due to the suppression of O 2*p*-Co^{3+} hybridization, similar to what has been reported in literature and other protonated systems. Furthermore, the broader region above 533–543 eV can be assigned to oxygen 2*p* orbitals in hybridization with transition metal 4*s* and 4*p* bands. Upon proton incorporation, this broad structural region shows the appearance of spectral features denoting hydroxyl bonds [7,27], as marked with the blue region in Fig. 4(c).

Figure 4's low panels exhibit the XAS results for NCO_{LP} pristine (3, 100, 2), (4, 100, 0.5) and the fully protonated NCO_{LP} (4, 100, 2) films at the Co L_{23} edge, Ni L_{23} edge, and O K edge, respectively. Predicting and understanding the cation distribution in NCO are still in debate [15,28,29]. The XAS spectra at the Co L_{23} edge and the Ni L_{23} edge are similar for pristine NCO_{LP} and NCO_{HP} samples, indicating the mixed 2+ and 3+ valence states for both Ni and Co ions [Figs. 4(a) and 4(e)]. However, distinct intensity changes have been observed at all three hybridized peaks of the O K edge, indicating that the cation inversion exists in both Ni and Co ions. This confirms the change of cation distribution upon low P_{O_2}, as suggested by electrical and magnetic transport measurements. With a lower P_{O_2}, peak III exhibits a negligible absorption intensity, implying that the Ni^{2+} concentration is relatively small, i.e., O_h-Ni^{2+} ions are exchanged with T_d-Ni^{3+} ions. Meanwhile, peak II possesses an enhanced absorption intensity, which can be ascribed to the losing of electrons originated from the partial T_d-Co^{2+} sites and O_h-Co^{3+} transformation. The tendency is consistent with the quantitative evaluation of the composition identification at different P_{O_2} resolved by resonant x-ray diffraction measurements [19] as well as the density function theory calculations [30]. We further note that the cation distribution not only varies the valence state but also the spin state configurations, where the partial T_d-Co^{2+} ($S = 3/2$) to O_h-Co^{3+} ($S = 0$) could be the microscopic mechanism for the reduced total magnetization and anisotropic field in pristine NCO_{LP} films.

After the ILG treatments, the core-level electronic state evolutions at Ni and Co sites are also similar to those of the NCO_{HP} samples, where the Ni L_{23}-edge spectra changes fully to reduced Ni^{2+} valence state with the initial (3, 100, 2) treatment as shown in Fig. 4(e). This confirms that the Ni ions near the E_F show the prior $Ni^{3+} \rightarrow Ni^{2+}$ response, whereas the Co ions exhibit a stepwise $Co^{3+} \rightarrow Co^{2+}$ evolution [22]. With the same ILG (3, 100 °C, 2) treatment, the Co valence states are distinct for protonated NCO_{HP} and NCO_{LP} films. The protonated NCO_{HP} film shows the dominant Co^{2+} valence state. However, the Co L_{23}-edge XAS spectra for NCO_{LP} (3, 100, 2) film shows a broad peak with a mixture of Co^{2+} and Co^{3+}. This verifies previous results that a higher energy barrier is necessary to fully protonate NCO_{LP} films. We speculate the influence of cation distribution on proton insertion dynamics as follows. Cation disorder exists at O_h-Ni^{2+} and T_d-Co^{2+} sites, resulting in Ni at T_d sites and more Co at O_h sites. This corresponds to a mixture structure of NCO films composed of inverse spinel (Ni with only O_h symmetry) and normal spinel (Ni with T_d symmetry). The higher energy barrier necessary to protonate NCO_{LP} might be related to the short relaxation time due to the increased concentration of heterogenous scattering centers which slows down the hydrogen diffusion dynamics in the relaxation time approximation. This will be further understood through the diffusion coefficient analyses as will be presented below.

E. Diffusion coefficient in complex NCO films

Figure 5 shows the Nyquist plots of the impedance spectra at opencircuit condition for pristine NCO_{HP} and NCO_{LP} films, as well as films at different ILG conditions. The spectra consist typically of a semicircle in a high frequency region from 0.1 Hz to 100 kHz using the CHI660E electrochemical workstation. The AC signal amplitude is 5 mV. The data is best fitted in an equivalent circuit of four elements with a CDC code, as shown in the inset of Fig. 5(b). The equation for the calculation of diffusion coefficient (D) values by EIS can be expressed as $D = R^2T^2/2n^2A^2F^4C^2\sigma^2$, where R is the gas constant, T is the temperature in unit of Kelvin, A is the electrode area, n is the number of electrons transferred during the reaction, F is the Faraday constant, C is the H ionophore phase concentration which can be deduced from the material density and the molecular weight, and σ is the Warburg factor which is obtained from the slope of Z' vs $\omega^{-1/2}$ curve. The σ value serves as the only variable for D calculation. By substituting the σ values, the calculated D values are in the range of 7.90×10^{-12} - 2.91×10^{-10} cm^2 s^{-1}. We note that the EIS results represent the combined electronic

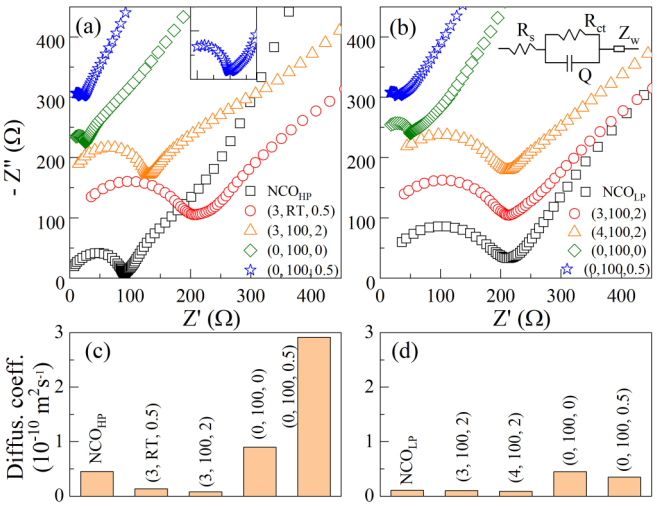

FIG. 5. Panels (a) and (b):Impedance spectra for NCO_{HP}, NCO_{LP} at different representative stages with frequency between 0.01 Hz to 100 kHz, respectively. Inset of panel (b) illustrates the equivalence circuits used for fitting the impedance spectra. Panels (c) and (d) exhibits the calculated hydrogen diffusion coefficients at different ILG treatment conditions for (c) NCO_{HP} and (d) NCO_{LP} set of films.

and ionic contributions. Generally, the low-frequency region mainly depends on the electronic transportation whereas the high-frequency region is dominated by the ionic motion. The D value is calculated from the slope of the Nyquist plots at the low-frequency region where the ionic contribution dominates. Compared with NCO_{HP}, pristine NCO_{LP} displays a smaller D value, where the poor proton diffusion can be ascribed to the increased amount of cation disorders, suggesting that cation disorders make against proton insertion through ILG approach.

Figures 5(a)–5(d) also exhibit the impedance spectra and the calculated D values of NCO_{HP} and NCO_{LP} films measured at different temperatures and periods. For NCO_{HP} films, the protonated (3, RT, 0.5) film displays a slightly reduced D value, which decreases further with $D \approx 7.90\text{x}10^{-12}$ cm^2 s^{-1} for the fully protonated H_2NCO film after (3, 100, 2) treatment. This tendency can be related to the more localized states in protonated films. A similar tendency has also been resolved in NCO_{LP} to the fully protonated film with (4, 100, 2) treatment conditions.

To further investigate the influence of temperature on proton insertion, we provided the temperature dependent EIS measurement at elevated temperature with a different time period using the water heating method. The warburg factor of the NCO_{HP} sample at a high temperature of 100° decreases more than three times, corresponding to the enhanced D value of more than one order of magnitude. We note that the D values measured at different treatment conditions in Fig. 5 were performed without dc gating voltage due to the setup limit; the D values do not represent the hydrogen diffusion in the ILG treated films but clearly support the temperature enhanced proton diffusion processes in NCO_{HP} films. However, the D values of NCO_{LP} shows a relatively small increase at elevated temperature, indicating a higher energy barrier is necessary for promoting the proton diffusion in NCO_{LP}, which deserves further theoretical inputs.

IV. CONCLUSIONS

In conclusion, we investigate the local electronic structure and the proton insertion dynamics through ILG approach in epitaxial spinel NCO films deposited at different P_{O_2} of 300 mTorr (denoted as NCO_{HP}) and 50 mTorr (denoted as NCO_{LP}). Detailed electric and magnetic transport results reveal that the dominant structural variation originates from the influences of cation distribution rather than oxygen vacancies in NCO_{LP} films. The difference of local electronic structure resolved by transition metal Co L_{23}-edge and Ni L_{23}-edge XAS spectra is not obvious for NCO deposited at high and low P_{O_2}. However, distinct XAS spectra at the prepeak region of the O K edge have been observed, which further suggest two couples of cation inversion between O_h-Ni^{2+} and T_d-Ni^{3+}, as well as between T_d-Co^{2+} and O_h-Co^{3+} sites. The spin configuration transition due to cation inversion at Co sites can be served as the origin for the reduced total magnetic moment and the reduced magnetic anisotropic field.

Toward effectively utilizing spinel oxides in emerging technologies through ILG approach, we further provide systematic investigations of the local structural variations of NCO_{HP} and NCO_{LP} films in different ILG treatment conditions. Our results show the robust ionic reduction procedure, i.e., the Ni ions near the E_F exhibit a prior Ni^{3+} to Ni^{2+} reduction, whereas the Co ions at different coordinated sites show the gradual $Co^{3+} \rightarrow Co^{2+}$ reduction procedure. However, with the same gating conditions as (3, 100, 2), the NCO_{HP} films are fully protonated as H_2NCO with insulating and antiferromagnetic behaviors. The NCO_{LP} exhibit the dominant Ni^{2+} and the partial reduction of Co^{3+}. Therefore, more stringent conditions are necessary for fully protonating NCO_{LP} films, which can be ascribed to the short relaxation time and poor diffusion coefficient accompanying with enhanced cation disorders in the relaxation time approximation. Certain amount of cation disorders make against proton insertion through ILG approach. Our studies advance the fundamental understanding of the spinel oxide with different cation distribution and shed light on the manipulation of the ground state in spinel oxides toward spintronic applications via ILG controlled protonation.

ACKNOWLEDGMENTS

This work was supported by the National Science Foundation of Fujian Province of China (No. 2022J01007), the National Natural Science Foundation of China (No. U22B20132, No. 11972136, No. 12174270, and No. 11704317), as well as the Fundamental Research Funds for Central Universities (Grant No. 20720210018). We also acknowledge the beamline scientists at the Magnetic Circular Dichroism beamline (BL12B) of the National Synchrotron Radiation Laboratory (NSRL)and the 4B9B beamline at the Beijing Synchrotron Radiation Facility (BSRF) for the approval of the beamtime and the kind assistances during the measurements.

[1] A. S. Dhoot, C. Israel, X. Moya, N. D. Mathur, and R. H. Friend, Phys. Rev. Lett. **102**, 136402 (2009).

[2] M. Nakano, K. Shibuya, D. Okuyama, T. Hatano, S. Ono, M. Kawasaki, Y. Iwasa, and Y. Tokura, Nature (London) **487**, 459 (2012).

[3] Y. Yamada, K. Ueno, T. Fukumura, H. T. Yuan, H. Shimotani, Y. Iwasa, L. Gu, S. Tsukimoto, Y. Ikuhara, and M. Kawasaki, Science **332**, 1065 (2011).

[4] K. Ueno, S. Nakamura, H. Shimotani, A. Ohtomo, N. Kimura, T. Nojima, H. Aoki, Y. Iwasa, and M. Kawasaki, Nat. Mater. **7**, 855 (2008).

[5] A. T. Bollinger, G. Dubuis, J. Yoon, D. Pavuna, J. Misewich, and I. Božović, Nature (London) **472**, 458 (2011).

[6] B. Lei, J. H. Cui, Z. J. Xiang, C. Shang, N. Z. Wang, G. J. Ye, X. G. Luo, T. Wu, Z. Sun, and X. H. Chen, Phys. Rev. Lett. **116**, 077002 (2016).

[7] N. Lu, P. Zhang, Q. Zhang, R. Qiao, Q. He, H.-B. Li, Y. Wang, J. Guo, D. Zhang, Z. Duan, Z. Li, M. Wang, S. Yang, M. Yan, E. Arenholz, S. Zhou, W. Yang, L. Gu, C.-W. Nan, J. Wu *et al.*, Nature (London) **546**, 124 (2017).

[8] Z. Li, S. Shen, Z. Tian, K. Hwangbo, M. Wang, Y. Wang, F. M. Bartram, L. He, Y. Lyu, Y. Dong, G. Wan, H. Li, N. Lu, J. Zang, H. Zhou, E. Arenholz, Q. He, L. Yang, W. Luo, and P. Yu, Nat. Commun. **11**, 184 (2020).

[9] S. Shen, Z. Li, Z. Tian, W. Luo, S. Okamoto, and P. Yu, Phys. Rev. X **11**, 021018 (2021).

[10] J. Song, Y. Chen, X. Chen, H. Wang, T. Khan, F. Han, J. Zhang, H. Huang, J. Zhang, H. Zhang, H. Zhang, X. Yan, S. Qi, F. Hu, B. Shen, R. Yu, and J. Sun, Phys. Rev. Appl. **12**, 054016 (2019).

[11] J. Song, Y. Chen, X. Chen, T. Khan, F. Han, J. Zhang, H. Huang, H. Zhang, W. Shi, S. Qi, F. Hu, B. Shen, and J. Sun, Phys. Rev. Appl. **14**, 024062 (2020).

[12] D. Yi, Y. Wang, O. M. J. van't Erve, L. Xu, H. Yuan, M. J. Veit, P. P. Balakrishnan, Y. Choi, A. T. NDiaye, P. Shafer, E. Arenholz, A. Grutter, H. Xu, P. Yu, B. T. Jonker, and Y. Suzuki, Nat. Commun. **11**, 902 (2020).

[13] L. Hu, L. Wu, M. Liao, and X. Fang, Adv. Mater. **23**, 1988 (2011).

[14] Y. Li, P. Hasin, and Y. Wu, Adv. Mater. **22**, 1926 (2010).

[15] X. Chen, X. Zhang, M.-G. Han, L. Zhang, Y. Zhu, X. Xu, and X. Hong, Adv. Mater. **31**, 1805260 (2019).

[16] J. F. Marco, J. R. Gancedo, M. Gracia, J. L. Gautier, E. I. Ríos, H. M. Palmer, C. Greaves, and F. J. Berry, J. Mater. Chem. **11**, 3087 (2001).

[17] M. Xue, X. Chen, S. Ding, Z. Liang, Y. Peng, X. Li, L. Zha, W. Yang, J. Han, S. Liu, H. Du, C. Wang, and J. Yang, ACS Appl. Electron. Mater. **2**, 3964 (2020).

[18] X. C. Huang, W.-W. Li, S. Zhang, F. E. Oropeza, G. Gorni, V. A. de la Peña-O'Shea, T.-L. Lee, M. Wu, L.-S. Wang, D.-C. Qi, L. Qiao, J. Cheng, and K. H. L. Zhang, Phys. Rev. B **104**, 125136 (2021).

[19] Y. Shen, D. Kan, Z. Tan, Y. Wakabayashi, and Y. Shimakawa, Phys. Rev. B **101**, 094412 (2020).

[20] D. Kan, L. Xie, and Y. Shimakawa, Phys. Rev. B **104**, 134407 (2021).

[21] M. Wang, X. Sui, Y. Wang, Y.-H. Juan, Y. Lyu, H. Peng, T. Huang, S. Shen, C. Guo, J. Zhang, Z. Li, H.-B. Li, N. Lu, A. T. N'Diaye, E. Arenholz, S. Zhou, Q. He, Y.-H. Chu, W. Duan, and P. Yu, Adv. Mater. **31**, 1900458 (2019).

[22] M. Wu, X. Huang, Y. Li, H. Luo, J. Shi, K. H. L. Zhang, P. Han, S. Hu, T. Deng, Y. Du, L. Chen, H.-Q. Wang, and J. Kang, Phys. Rev. B **107**, 125107 (2023).

[23] H.-B. Li, F. Lou, Y. Wang, Y. Zhang, Q. Zhang, D. Wu, Z. Li, M. Wang, T. Huang, Y. Lyu, J. Guo, T. Chen, Y. Wu, E. Arenholz, N. Lu, N. Wang, Q. He, L. Gu, J. Zhu, C.-W. Nan *et al.*, Adv. Sci. **6**, 1901432 (2019).

[24] I. Suzuki, D. Kan, M. Kitamura, Y. Shen, K. Horiba, and Y. Shimakawa, J. Appl. Phys. **127**, 203903 (2020).

[25] C. Mellinger, J. Waybright, X. Zhang, C. Schmidt, and X. Xu, Phys. Rev. B **101**, 014413 (2020).

[26] D. Kan, M. Mizumaki, M. Kitamura, Y. Kotani, Y. Shen, I. Suzuki, K. Horiba, and Y. Shimakawa, Phys. Rev. B **101**, 224434 (2020).

[27] X. Shan, D. S. Charles, Y. Lei, R. Qiao, G. Wang, W. Yang, M. Feygenson, D. Su, and X. Teng, Nat. Commun. **7**, 13370 (2016).

[28] M. N. Iliev, P. Silwal, B. Loukya, R. Datta, D. H. Kim, N. D. Todorov, N. Pachauri, and A. Gupta, J. Appl. Phys. **114**, 033514 (2013).

[29] Y. Bitla, Y.-Y. Chin, J.-C. Lin, C. N. Van, R. Liu, Y. Zhu, H.-J. Liu, Q. Zhan, H.-J. Lin, C.-T. Chen, Y.-H. Chu, and Q. He, Sci. Rep. **5**, 15201 (2015).

[30] C. Wu, L. liu, R. Xu, K. Zhang, C. Zhen, L. Ma, and D. Hou, Mater. Sci. Eng.: B **263**, 114886 (2021).